Magmatism at oceanic core complexes on the ultraslow Southwest Indian Ridge: Insights from near-seafloor magnetics

Fei Zhou, Jérôme Dyment, Chunhui Tao, Tao Wu

Magmatism at oceanic core complexes on the ultraslow Southwest Indian Ridge: insights from near-seafloor magnetics

Fei Zhou[1], Jérôme Dyment[1*], Chunhui Tao[2*], Tao Wu[2]

[1]Université de Paris, Institut de physique du globe de Paris, CNRS, F-75005 Paris, France

[2]Key Laboratory of Submarine Geosciences, MNR, Second Institute of Oceanography, MNR, 310012 Hangzhou, China

Corresponding authors: Jérôme Dyment, jdy@ipgp.fr and Chunhui Tao, taochunhuimail@163.com

ABSTRACT

Oceanic core complexes (OCCs) and detachment faults (DFs) play a key role in crustal accretion at slow and ultraslow spreading centers. We investigate the effect of different magma supply at three OCCs of the Southwest Indian Ridge (SWIR) using high-resolution deep-sea bathymetric and magnetic data. The average equivalent thickness of extrusive basalt deduced from the magnetic anomalies, a proxy for the magma supply, decreases from Yuhuang (49.25°E) to Longqi (49.65°E) to Junhui (51.75°E) OCCs. Conversely, serpentinite outcrops become more abundant, the domal OCC morphology flattens as the footwall rotation (measured by the magnetization vector inclination) increases, and hydrothermal evidences become sparse. Combined with results from the amagmatic Easternmost SWIR, our study shows that the magma supply controls the character and evolution of the OCCs and DFs on the SWIR.

INTRODUCTION

As an essential constituent of slow and ultraslow spreading centers, Oceanic Core Complexes (OCCs) result in asymmetric flanks, corrugated seafloor, and mantle rocks exhumation. They have not only been found at magma-starved ridge segment ends (Cann et al., 1997; Tucholke et al., 1998; Blackman et al., 1998) but are widespread and account for 50% of the recent seafloor formed at the Mid-Atlantic Ridge (MAR) (Smith et al., 2006; Escartín et al., 2008). Numerical models suggest that magmatism plays a major role in the development of the OCCs (Buck et al., 2005; Tucholke et al., 2008; Olive et al., 2010). In contrast, OCCs are still poorly known at ultraslow spreading ridges. An end-member is the Southwest Indian Ridge (SWIR) east of Melville Fracture Zone (FZ), a nearly amagmatic spreading center which exposes smooth seafloor interpreted as the remnants of DF footwalls (Cannat et al., 2006). Seafloor spreading is purely tectonic there. Conversely, the SWIR exhibits a more robust magma supply further west (Sauter et al., 2001). In this area, between the Indomed and Gallieni FZs (Fig. 1A), the shallower water depth and lower Mantle Bouguer Anomaly indicate a thicker crust and hotter

mantle, and the higher amplitude of the Central Magnetic Anomaly a thicker extrusive basalt layer. We use high-resolution bathymetry and magnetic data to investigate three OCCs, the Yuhuang, Longqi, and Junhui OCCs, in this area, and show that the morphology, magnetic signature, and evolution of these OCCs are tightly related to the magma supply.

DATA AND METHODS

Near-bottom bathymetry and magnetic data were acquired by "*Qianlong II*" Autonomous Underwater Vehicle (AUV) during DY-43, 49 and 52 cruises from 2014 to 2020. The AUV collected data at an altitude of ~100 m above seafloor, with a sampling interval of 1 m along lines 400 m apart. Noise introduced by attitude variation is reduced by the method of (Tao et al., 2018), and the International Geomagnetic Reference Field (IGRF) model (Thébault et al., 2015) is removed. The magnetic anomaly is gridded at 100 m×100 m interval and inverted to equivalent magnetization by using regularized minimum residual method (See details in Data Repository) assuming a magnetized layer 100 m-thick below the seafloor. Because the anomaly is measured on an uneven observation surface and for the sake of resolution, we calculate the Reduced-To-the-Pole (RTP) magnetic anomaly by forward modelling from the equivalent magnetization (Szitkar et al., 2014).

RESULTS

Geological description of the OCCs

We interpret the components of the three OCCs (breakaway, detachment surface, termination) on the shipboard and AUV bathymetry following the criteria of Smith et al. (2006).

Yuhuang OCC (Fig. 1B; Suppl. Fig. DR1) strikes in ENE direction, slightly oblique to the E-W axial volcanic zone (AVZ). It extends ~6 km along the spreading direction and drops ~1.5 km in elevation from breakaway to termination. The termination separates volcanic terrains to the North and the detachment surface where serpentinite samples were dredged. Further south a chaotic volcanic area, where dredges recovered basalt, hosts a hydrothermal field with large sulfide deposits (Tao et al., 2014; Liao et al., 2018).

Longqi OCC (Fig. 1C; Suppl. Fig. DR1) extends ~15 and ~4 km along and across axis, respectively. South of the termination, the detachment surface displays corrugations in the spreading direction. Mass wasting is clearly seen on the western end of the OCC. Basalt was dredged all over the area, but serpentinite was only dredged on the detachment surface. High temperature hydrothermal site Longqi-1 was found on the hanging wall (Tao et al., 2012; 2020), whereas inactive site Longqi-3 was found in the chaotic area separating the detachment surface and the breakaway. Further south, an older volcanic zone and a large DF are identified on the regional bathymetry (Fig. DR1).

Junhui OCC (Fig. 1D; Suppl. Fig. DR1), the easternmost one, extends ~9 and ~6 km along and across axis, respectively. The detachment footwall is quite flat. Mass wasting is

observed in the middle of the area, and smooth seafloor is tentatively identified to the West (Fig. 1D and F). Basalt has been dredged east of the area, and serpentinite on the detachment surface only. No hydrothermal field has been reported yet.

Magnetization Inclination and Footwall Rotation

The magnetization acquired by young oceanic basalt at mid-ocean ridges within the last million year is approximately parallel to the present-day geomagnetic field. However, the magnetization vector direction can be affected by subsequent tectonics, such as DFs, as observed on the MAR at 26°N (Szitkar and Dyment, 2015; Szitkar et al., 2019). It is not easy to estimate the footwall rotation at the observed OCCs in the absence of any specific structural or paleomagnetic measurements (e.g., Morris et al., 2009). To address this problem, we explore the full range of possible remanent magnetization directions, calculate their corresponding RTP anomalies and select the range of inclinations that make the anomalies centered on its causative source, in general basaltic features such as the linear breakaways. OCC footwall rotation axes are generally orthogonal to the spreading direction, i.e. broadly east-west for the broadly north-south spreading SWIR. Following the dipole field hypothesis, the magnetization vector trends North and its rotation around a perpendicular axis allows the rotation angle to be estimated directly from the inclination data. The inclinations that properly deskew the observed anomalies are -75°~-105° (average -90°), -75°~-120° (av. -97.5°), and -85°~-135° (av. -110°) for Yuhuang, Longqi, and Junhui OCCs, respectively. Because the inclination of the dipole field is -57° in the area, we estimate the amount of rotation as 33°±15°, 40.5°±22.5°, and 53°±25° for the Yuhuang, Longqi, and Junhui, respectively.

RTP Magnetic Anomaly

RTP anomaly over the Yuhuang OCC trends NE-SW, parallel to the structural orientation (Fig. 1B and E). The strong linear positive anomaly separates the area in three parts, from North to South (1) low and slightly negative anomaly reflecting the weak induced magnetization of recovered serpentinites; (2) strong positive linear anomaly associated with basalt, suggesting that the contrast of magnetic signature with the northern part corresponds to a lithological boundary; and (3) strong negative anomalies associated with basalt, suggesting that the transition corresponds to a polarity boundary, most likely the Brunhes-Matuyama boundary (0.78 Ma; e.g., Cande and Kent, 1995). The OCC therefore initiated in the late stage of the Matuyama period. RTP anomaly over the Longqi OCC is generally oriented E-W (Fig. 1C and F). In the north-west corner, around Longqi-1 hydrothermal vent, a strong positive anomaly indicates recent and abundant volcanism. A weak negative magnetic anomaly characterizes serpentinite and the detachment surface. Further south, the breakaway, a bathymetric high with basalt outcrops, is marked by three E-W lineated anomalies, from north to south a weak positive anomaly, a strong negative anomaly, and a strong positive anomaly. We interpret this succession of anomalies as a geomagnetic polarity sequence recorded by the remanent magnetization of basalt. The transitions

north and south of the strong negative anomaly correspond to the polarity reversals between the Brunhes and Matuyama periods (0.78 Ma), and between the younger part of the Matuyama period and the Jaramillo normal episode (0.99 Ma), respectively. The southern side of the strong positive anomaly thus records the older end of the Jaramillo episode (1.07 Ma) and is therefore underlain by basalt although no sample is available to confirm this hypothesis. The Jaramillo anomaly further continues to the west (Fig.1F), as interpreted by Wu et al. (2021). The elevated area extending further south toward the termination of the older DF is also probably made of volcanics formed during the Matuyama period (Tao et al., 2020). Conversely, the weaker transition observed north of the weak positive anomaly corresponds to the lithological transition between serpentinites and basalt. These observations indicate that the OCC initiated during the Jaramillo episode between 0.99~1.07 Ma.

RTP anomaly over the Junhui OCC (Fig. 1D and G) shows weak negative anomalies. In the West, the inferred smooth seafloor does not display any significant signal. In the southeastern corner of the area, a negative E-W anomaly near the breakaway is interpreted as a polarity boundary, suggesting that this OCC also initiated during the Late Matuyama period. Northward, the lithological boundary between basalt and serpentinite is inferred from a weak E-W anomaly.

Modeling

Extrusive basalt is the dominant source of marine magnetic anomalies, with additional contribution of the deeper crust and/or uppermost mantle at slower spreading rates (e.g., Dyment and Arkani-Hamed, 1995; Dyment et al., 1997). Magnetics therefore offer an indirect means to evaluate the amount of basalt and other magmatic products, and *in fine* to approach the magma supply for comparison among our study areas. To this end, we use forward modeling to compute the thickness of extrusive basalt that best explains the observed anomalies. However, in order to alleviate the fundamental non-uniqueness of potential field methods, we have to adopt several simplifying hypotheses to determine what we call the equivalent thickness of extrusive basalt (ETB), i.e. the thickness of extrusive basalt if our simplifying hypotheses were correct. We assume that (1) the magnetized crust is 1 km-thick beneath the seafloor – indeed deeper sources have negligible magnetic effect at 100 m altitude; (2) the magnetized crust is made of two layers: an extrusive basalt layer overlying a serpentinite layer; (3) the basalt layer bears only thermo-remanent magnetization of 15A/m (See Data Repository Section D); (4) the serpentinite layer bears only induced magnetization of 2A/m (e.g., Oufi et al., 2002). We neglect geological features that do not have a significant magnetic effect. For instance, rubbles on the detachment surface are randomly oriented and the contribution of their magnetization to the anomaly cancels out. The deformed fault zone may bear a consistent magnetization acquired during frictional heating but its thickness is negligible.

Within the above hypotheses, we adjust the depth of the basalt-serpentinite interface, reflected by the thickness of the basalt layer, to account for the RTP anomaly. On detachment surfaces, the ETB is generally negligible, less than 100 m-thick. The polarity of the basalt

remanent magnetization is set to normal (respectively reversed) where the RTP anomaly is positive (resp. negative) (See Data Repository Fig. DR3).

The modeling results indicate that the synthetic and observed anomalies are in good agreement (Fig. 2). We estimate the average amount of basalt from the ETB (See Data Repository Section E) to 77.4±10.7 m (Yuhuang), 68.5±14.2 m (Longqi), and 30.1±22.1 m (Junhui). The amount of basalt decreases gradually from Yuhuang to Longqi to Junhui OCCs. As the spreading rate is the same for the three OCCs, these values are representative of the magma supply. The Yuhuang OCC is more magmatic than the Longqi OCC, and much more magmatic than the Junhui OCC.

The ETB varies in average (on sections) from 16% (Yuhuang and Longqi) to 10% (Junhui) of the 500 m-thick basalt layer of standard oceanic crust, suggesting that this proportion of the crustal accretion is magmatic in the study area. This estimate only reflects the crustal accretion on the SWIR southern flank, as no clear OCC appears on the shipboard multibeam bathymetry of the northern flank for the considered period. In absence of high resolution bathymetric and magnetic data, no inference can be drawn for this flank, and therefore the whole area, for the last ~1.5 Ma.

DISCUSSION

Our observations and result suggest that the geology and magnetic signature of the OCCs are causally linked to the magma supply. In decreasing order of the magma supply, from Yuhuang to Longqi to Junhui OCCs, we observe (1) gradually flattening footwall surfaces as reflected by the increasing footwall rotation angles, (2) more abundant serpentinite outcrops, and (3) less evidences of hydrothermalism, whereas (4) the RTP anomalies related to magnetic polarity become weaker, less linear, and cover less area. For even lower magma supply, previous studies of the easternmost SWIR in a nearly amagmatic environment (Cannat et al., 2006, 2019; Sauter et al., 2013) showed smooth footwall surfaces made of serpentinite on both flanks, with consistently weak magnetic anomalies. Figure 3 presents four schematic sections in decreasing order of magmatism. The more magmatic Yuhuang OCC (Fig. 3A) is probably underlain by strong gabbroic cores, resulting from the capture of gabbroic bodies by the footwall near the Lithosphere-Asthenosphere boundary, as reflected by its broad dome morphology and smaller footwall rotation (MacLeod et al., 2009). At the less magmatic Longqi OCC (Fig. 3B), the footwall may include less gabbro bodies resulting in a less-marked dome structure (Ciazela et al., 2015), although hot gabbro bodies have not been detected so far by seismic methods in this area (Tao et al., 2020). Furthermore, the observation of two OCCs and an intermediate volcanic zone supports the alternance of detachment and magmatic spreading. The even less magmatic Junhui OCC (Fig. 3C) shows a flatter and longer serpentinite outcrop, suggesting that the footwall only captures rare gabbroic bodies. For amagmatic spreading as the easternmost SWIR (Fig. 3D), the footwall of the DF is not even defined as an OCC *sensu stricto* because it does not display the typical dome morphology due to its exclusive serpentinite composition. There, DFs are purely

tectonic, with the previously active DF being terminated by the initiation, across its footwall, of a new DF with opposite slope (Sauter et al., 2013).

Our results suggest that magmatism and tectonics are controlling in various degrees the Yuhuang, Longqi, and Junhui OCCs, which all initiated in response to a decreasing magma supply at the ridge axis and will probably end as magmatism gradually resumes. The magma supply affects characters of the OCCs such as morphology, serpentinite outcrops and underlaying gabbro bodies, hosted hydrothermal vents, and the magnetic signature. Magmatism in this area results in the initiation and termination of detachments separated by magmatic spreading periods, in alternance. Conversely, amagmatic spreading results in the purely tectonic exhumation of serpentinite on alternating DFs, as observed in the Easternmost SWIR. The variability of OCCs and DFs along the ultraslow spreading centers may reflect the heterogeneity of the along-axis magma supply and therefore offers a proxy to this parameter.

ACKNOWLEDGMENTS

We thank all the members of DY-43,49, 52 cruises and the AUV team. The data collection was supported by 2018YFC0309901 and 2018YFC0309903 and by the COMRA Major Project DY135-S1-01-01. Fei Zhou is funded by China Scholarship Council 201906170047. We thank Editor J. Dickens, A. Morris and four anonymous reviewers for their contribution to improve the paper. Correspondence on methodology and results of the magnetic study should be sent to JD, and on data availability and the regional project to CT. This is IPGP contribution 4256.

REFERENCES

Blackman, D.K., Cann, J.R., Janssen, B., and Smith, D.K., 1998, Origin of extensional core complexes: Evidence from the Mid-Atlantic Ridge at Atlantis Fracture Zone: Journal of Geophysical Research: Solid Earth, v. 103, p. 21315–21333, doi:10.1029/98JB01756.

Buck, W.R., Lavier, L.L., and Poliakov, A.N.B., 2005, Modes of faulting at mid-ocean ridges: Nature, v. 434, p. 719–723, doi:10.1038/nature03358.

Cande, S.C., and Kent, D.V., 1995, Revised calibration of the geomagnetic polarity timescale for the Late Cretaceous and Cenozoic: Journal of Geophysical Research: Solid Earth, v. 100, p. 6093–6095, doi:10.1029/94JB03098.

Cann, J.R., Blackman, D.K., Smith, D.K., McAllister, E., Janssen, B., Mello, S., Avgerinos, E., Pascoe, A.R., and Escartin, J., 1997, Corrugated slip surfaces formed at ridge–transform intersections on the Mid-Atlantic Ridge: Nature, v. 385, p. 329–332, doi:10.1038/385329a0.

Cannat, M., Sauter, D., Lavier, L., Bickert, M., Momoh, E., and Leroy, S., 2019, On spreading modes and magma supply at slow and ultraslow mid-ocean ridges: Earth and Planetary Science Letters, v. 519, p. 223–233, doi:10.1016/j.epsl.2019.05.012.

Cannat, M., Sauter, D., Mendel, V., Ruellan, E., Okino, K., Escartin, J., Combier, V., and Baala, M., 2006, Modes of seafloor generation at a melt-poor ultraslow-spreading ridge: Geology, v. 34, p. 605, doi:10.1130/G22486.1.

Ciazela, J., Koepke, J., Dick, H.J.B., and Muszynski, A., 2015, Mantle rock exposures at oceanic core complexes along mid-ocean ridges: Geologos, v. 21, p. 207-231, doi:10.1515/logos-2015-0017.

Dyment, J., and Arkani-Hamed, J., 1995, Spreading-rate-dependent magnetization of the oceanic lithosphere inferred from the anomalous skewness of marine magnetic anomalies: Geophysical Journal International, v. 121, p. 789–804, doi:10.1111/j.1365-246X.1995.tb06439.x.

Dyment, J., Arkani-Hamed, J., and Ghods, A., 1997, Contribution of serpentinized ultramafics to marine magnetic anomalies at slow and intermediate spreading centres: insights from the shape of the anomalies: Geophysical Journal International, v. 129, p. 691–701, doi:10.1111/j.1365-246X.1997.tb04504.x.

Escartín, J., Smith, D.K., Cann, J., Schouten, H., Langmuir, C.H., and Escrig, S., 2008, Central role of detachment faults in accretion of slow-spreading oceanic lithosphere: Nature, v. 455, p. 790–794, doi:10.1038/nature07333.

Liao, S., Tao, C., Li, H., Barriga, F.J.A.S., Liang, J., Yang, W., Yu, J., and Zhu, C., 2018, Bulk geochemistry, sulfur isotope characteristics of the Yuhuang-1 hydrothermal field on the ultraslow-spreading Southwest Indian Ridge: Ore Geology Reviews, v. 96, p. 13–27,

doi:10.1016/j.oregeorev.2018.04.007.

MacLeod, C.J., Searle, R.C., Murton, B.J., Casey, J.F., Mallows, C., Unsworth, S.C., Achenbach, K.L., and Harris, M., 2009, Life cycle of oceanic core complexes: Earth and Planetary Science Letters, p. 12.

Morris, A., Gee, J.S., Pressling, N., John, B.E., MacLeod, C.J., Grimes, C.B., and Searle, R.C., 2009, Footwall rotation in an oceanic core complex quantified using reoriented Integrated Ocean Drilling Program core samples: Earth and Planetary Science Letters, v. 287, p. 217–228, doi:10.1016/j.epsl.2009.08.007.

Olive, J.-A., Behn, M.D., and Tucholke, B.E., 2010, The structure of oceanic core complexes controlled by the depth distribution of magma emplacement: Nature Geoscience, v. 3, p. 491–495, doi:10.1038/ngeo888.

Oufi, O., Cannat, M., and Horen, H., 2002 Magnetic properties of variably serpentinized abyssal peridotites: Journal of Geophysical Research, v. 107, p. 2095, doi:10.1029/2001JB000549.

Sauter, D. et al., 2013, Continuous exhumation of mantle-derived rocks at the Southwest Indian Ridge for 11 million years: Nature Geoscience, v. 6, p. 314–320, doi:10.1038/ngeo1771.

Sauter, D., Patriat, P., Rommevaux-Jestin, C., Cannat, M., and Briais, A., 2001, The Southwest Indian Ridge between 49°15′E and 57°E: focused accretion and magma redistribution: Earth and Planetary Science Letters, v. 192, p. 303–317, doi:10.1016/S0012-821X(01)00455-1.

Smith, D.K., Cann, J.R., and Escartín, J., 2006, Widespread active detachment faulting and core complex formation near 13° N on the Mid-Atlantic Ridge: Nature, v. 442, p. 440–443, doi:10.1038/nature04950.

Szitkar, F., and Dyment, J., 2015, Near-seafloor magnetics reveal tectonic rotation and deep structure at the TAG (Trans-Atlantic Geotraverse) hydrothermal site (Mid-Atlantic Ridge, 26°N): Geology, v. 43, p. 87–90, doi:10.1130/G36086.1.

Szitkar, F., Dyment, J., Fouquet, Y., and Choi, Y., 2014, What causes low magnetization at basalt-hosted hydrothermal sites? Insights from inactive site Krasnov (MAR 16°38′N): Geochem. Geophys. Geosyst. 15, 1441–1451, doi:10.1002/2014GC005284.

Szitkar, F., Dyment, J., Petersen, S., Bialas, J., Klischies, M., Graber, S., Klaeschen, D., Yeo, I., and Murton, B.J., 2019, Detachment tectonics at Mid-Atlantic Ridge 26°N: Scientific Reports, v. 9, p. 11830, doi:10.1038/s41598-019-47974-z.

Tao, C. et al., 2012, First active hydrothermal vents on an ultraslow-spreading center: Southwest Indian Ridge: Geology, v. 40, p. 47–50, doi:10.1130/G32389.1.

Tao, C., Li, H., Jin, X., Zhou, J., Wu, T., He, Y., Deng, X., Gu, C., Zhang, G., and Liu, W., 2014, Seafloor hydrothermal activity and polymetallic sulfide exploration on the southwest Indian ridge: Chinese Science Bulletin, v. 59, p. 2266–2276, doi:10.1007/s11434-014-0182-0.

Tao, C. et al., 2020, Deep high-temperature hydrothermal circulation in a detachment faulting system on the ultra-slow spreading ridge: Nature Communications, v. 11, p. 1300,

doi:10.1038/s41467-020-15062-w.

Tao, W., Chunhui, T., Jinhui, Z., and Cai, L., 2018, Correction of tri-axial magnetometer interference caused by an autonomous underwater vehicle near-bottom platform: Ocean Engineering, v. 160, p. 68–77, doi:10.1016/j.oceaneng.2018.04.066.

Thébault, E. et al., 2015, International Geomagnetic Reference Field: the 12th generation: Earth, Planets and Space, v. 67, p. 79, doi:10.1186/s40623-015-0228-9.

Tucholke, B.E., Behn, M.D., Buck, W.R., and Lin, J., 2008, Role of melt supply in oceanic detachment faulting and formation of megamullions: Geology, v. 36, p. 455, doi:10.1130/G24639A.1.

Tucholke, B.E., Lin, J., and Kleinrock, M.C., 1998, Megamullions and mullion structure defining oceanic metamorphic core complexes on the Mid-Atlantic Ridge: Journal of Geophysical Research: Solid Earth, v. 103, p. 9857–9866, doi:10.1029/98JB00167.

Wu, T., Tivey, M.A., Tao, C., Zhang, J., Zhou, F., and Liu, Y., 2021, An intermittent detachment faulting system with a large sulfide deposit revealed by multi-scale magnetic surveys: Nature Communications, v. 12, p. 5642, doi:10.1038/s41467-021-25880-1.

FIGURE CAPTIONS

Figure 1. (A) Regional bathymetry from shipboard multibeam echo-sounders. Black boxes show AUV areas in (from west to east) Yuhuang, Longqi, and Junhui OCCs. Inset gives the location of study area. (B-D) High-resolution bathymetry of Yuhuang, Longqi, and Junhui areas. At Yuhuang OCC, no AUV bathymetry was acquired, and we display shipboard bathymetry instead. (E-G) RTP magnetic anomaly of Yuhuang, Longqi, and Junhui areas calculated through equivalent magnetization.

Figure 2. Forward modelling of the RTP magnetic anomalies on the three investigated areas. Each panel A-C and G-I shows, on top, a section across the structure resulting from forward modelling where green is serpentinite, red (blue) basalt with normal (reversed) polarity; and, on bottom, modelled (red) and observed (blue) RTP anomalies. The location of these section is indicated as black lines labelled 1 (panels A-C) and 2 (panels G-I) on maps in the middle column. These maps display the modelled RTP anomaly (color) superimposed on the bathymetry (shadows). See text for details on the forward modelling.

Figure 3. Synthetic cross-sections presenting OCCs and DFs from more to less magmatism as suggested by the averaged equivalent thickness of extrusive basalt. A), B), C) display interpretations of the Yuhuang, Longqi and Junhui OCCs. D) displays the interpretation of the amagmatic Easternmost SWIR after Cannat et al. (2019).

A)

37.0°S
37.2°S
37.4°S
37.6°S
37.8°S
38.0°S
38.2°S
49.0°E
49.5°E
50.0°E
50.5°E
51.0°E
51.5°E
52.0°E
I
G

Breakaway
Termination
Mass wasting
Lithological boundary
Magnetic polarity boundary
Basalt
Serpentinite
Axial volcanic ridge
Hydrothermal site
Hydrothermal plume
G: Gallieni fracture zone
I: Indomed fracture zone
B: Brunhes, M: Matuyama, J: Jaramillo magnetic polarity episodes
Location of sections in Figure 3

B)

1000 (m)
3500
49.32°E
49.29°E
49.26°E
49.23°E
37.92°S
37.95°S

C)

1000 (m)
3500
49.74°E
49.71°E
49.68°E
49.65°E
37.77°S
37.80°S
37.83°S

D)

1000 (m)
3500
51.75°E
51.72°E
51.69°E
37.44°S
37.47°S

E
N

Depth below sea level (m)
3500 3000 2500 2000 1500 1000

0 6 km

E)

FIG. 3A
B
M
1000 (m)
3500
49.32°E
49.29°E
49.26°E
49.23°E
37.92°S
37.95°S

F)

FIG. 3B
B
M
J
1000 (m)
3500
49.74°E
49.71°E
49.68°E
49.65°E
37.77°S
37.80°S
37.83°S

G)

FIG. 3C
M
B
1000 (m)
3500
51.75°E
51.72°E
51.69°E
37.44°S
37.47°S

RTP magnetic anomaly (nT)
-3000 -2000 -1000 0 1000 2000 3000

Profile 1

A)

Depth below sea level (m)

1000
2000
3000
4000

37.96°S 37.94°S 37.92°S 37.90°S

Latitude (°)

RTP magnetic anomaly (nT)

4000
2000
0
−2000
−4000

37.96°S 37.94°S 37.92°S 37.90°S

Latitude (°)

1 Yuhuang 2

D)

37.92°S

37.95°S

F)

49.23°E 49.26°E 49.29°E 49.32°E

Profile 2

G)

Depth below sea level (m)

1000
2000
3000
4000

37.96°S 37.94°S 37.92°S 37.90°S

Latitude (°)

RTP magnetic anomaly (nT)

4000
2000
0
−2000
−4000

37.96°S 37.94°S 37.92°S 37.90°S

Latitude (°)

B)

Depth below sea level (m)

1000
2000
3000
4000

37.84°S 37.82°S 37.80°S 37.78°S 37.76°S

Latitude (°)

RTP magnetic anomaly (nT)

4000
0
−4000

37.84°S 37.82°S 37.80°S 37.78°S 37.76°S

Latitude (°)

Longqi 1 2

E)

37.77°S

37.80°S

37.83°S

49.65°E 49.68°E 49.71°E 49.74°E

H)

Depth below sea level (m)

1000
2000
3000
4000

37.84°S 37.82°S 37.80°S 37.78°S 37.76°S

Latitude (°)

RTP magnetic anomaly (nT)

4000
0
−4000

37.84°S 37.82°S 37.80°S 37.78°S 37.76°S

Latitude (°)

C)

Depth below sea level (m)

1000
2000
3000
4000

37.48°S 37.46°S 37.44°S 37.42°S

Latitude (°)

RTP magnetic anomaly (nT)

4000
2000
0
−2000
−4000

37.48°S 37.46°S 37.44°S 37.42°S

Latitude (°)

Junhui 1 2

F)

37.44°S

37.47°S

51.69°E 51.72°E 51.75°E

I)

Depth below sea level (m)

1000
2000
3000
4000

37.48°S 37.46°S 37.44°S 37.42°S

Latitude (°)

RTP magnetic anomaly (nT)

4000
2000
0
−2000
−4000

37.48°S 37.46°S 37.44°S 37.42°S

Latitude (°)

Observed RTP

Modelled RTP

-3000 -2000 -1000 0 1000 2000 3000

RTP magnetic anomaly (nT)

Hydrothermal site

Hydrothermal plume

Serpentinite

Basalt

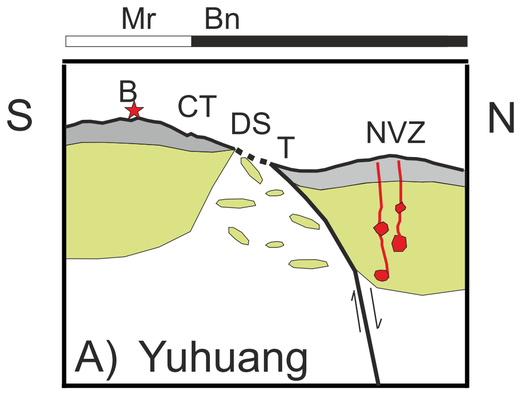

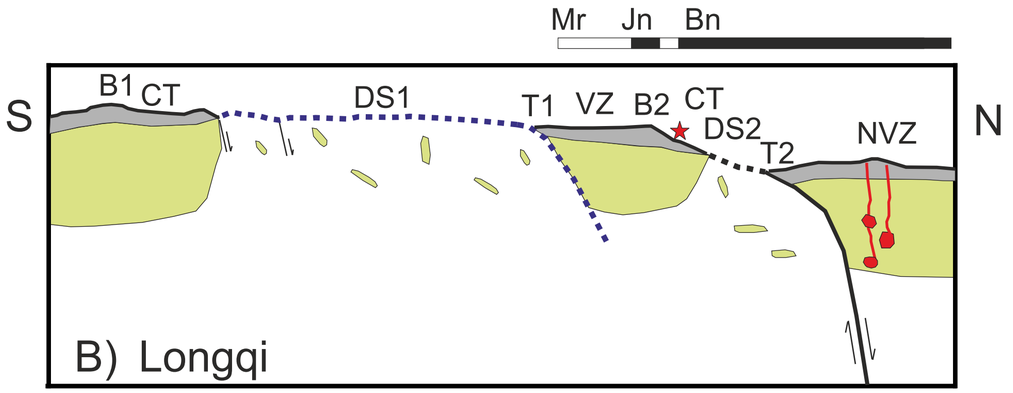

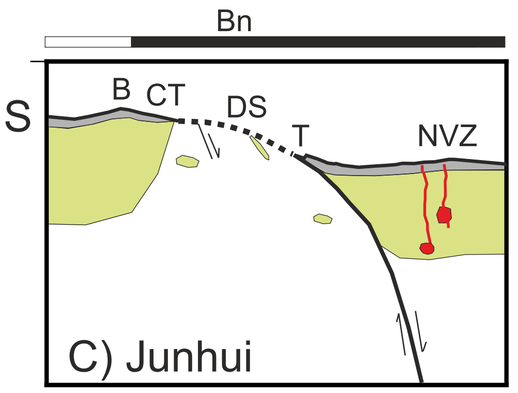

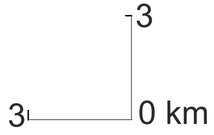

Cooled gabbro | Magma body | Basalt

Hydrothermal field | Dikes | Later faults

Detachment fault | Detachment surface

B: Breakaway T: Termination DS: Detachment surface

VZ: Volcanic zone NVZ: Neovolcanic zone CT: Chaotic terrain

Bn: Brunhes (normal) magnetic polarity episode 0-0.78 Ma

Mr: Matuyama (reverse) magnetic polarity episode 0.78-2.58 Ma

Jn: Jaramillo (normal) magnetic polarity episode 0.99-1.07 Ma